J. Fluid Mech. (2004), *vol.* 504, *pp.* 271–299. © 2004 Cambridge University Press
DOI: 10.1017/S0022112004008109 Printed in the United Kingdom

Verification of acoustic solitary waves

By N. SUGIMOTO, M. MASUDA, K. YAMASHITA AND H. HORIMOTO

Division of Nonlinear Mechanics, Department of Mechanical Science, Graduate School of Engineering Science, University of Osaka, Toyonaka, Osaka 560-8531, Japan

(Received 22 July 2003 and in revised form 18 November 2003)

Experiments and numerical simulations are carried out to verify the existence of the acoustic solitary wave in an air-filled tube with an array of Helmholtz resonators connected. Following up previous work (Sugimoto *et al.* 1999), the experiments are improved by using a newly designed piston driver to launch an initially plane pressure pulse and also by extending the tube length from 7.4 m to 10.6 m. To highlight the effect of the array of resonators, the case with no array is also examined in parallel. Direct and indirect checks are made to verify the existence of the solitary wave. The former compares the profiles and propagation speeds of pulses measured experimentally to the solitary-wave solution. The latter checks the validity of nonlinear wave equations in describing real wave evolution in the tube. Solving an initial-value problem numerically with weakly lossy effects of boundary layers and jet loss at the throat of the resonator, comparison is made between measured and simulated evolution. The validity of the equations in the lossy case is necessary to maintain the existence of the solitary wave in the lossless limit. It is revealed that nonlinear wave equations originally derived for unidirectional propagation in the tube can provide a good description of the real evolution, with some allowance for phase shifts on reflection at both ends of the tube. In particular, it turns out that the lossy effects are described quantitatively well. By establishing the validity of the equations, it is concluded that the acoustic solitary wave exists.

1. Introduction

The discovery of the acoustic solitary wave in air has attracted much attention (Physical Review Focus 1999; Hellemans 1999; Weiss 1999). This is perhaps because it originates in the study of the practical problem of suppressing shock in tunnels (Sugimoto 2001) and also academically because nonlinear acoustic waves usually evolve into shocks and no solitary waves have so far been believed to exist in air. This belief has been endorsed by the fact that air is a dissipative medium, not a dispersive one favourable to the generation of the solitary wave. In fact, it is still true that no solitary waves exist in open air.

As dispersion of acoustic waves is brought about by the presence of a boundary, a guided wave propagation is necessary if the solitary waves are to be generated. But weak dispersion resulting from non-uniformity of the cross-section of a tube or a hereditary effect due to a boundary layer on the tube wall fails to yield the solitary wave. But it has been revealed in theory that when a tube has a spatially periodic structure by connecting an array of Helmholtz resonators appropriately, acoustic solitary waves can be propagated (Sugimoto 1992, 1996). To confirm the theoretical findings, experiments have been performed (Sugimoto *et al.* 1999). This paper follows

up the previous work by making new experiments and also by numerical simulations to verify their existence.

An acoustic solitary wave is the steady and stable propagation of a localized pulse having a smooth profile free from a shock and consisting of a compression phase only. The propagation speed is slower than the linear sound speed, i.e. subsonic, but faster than a threshold value determined by a 'size parameter' of the array of Helmholtz resonators. At the upper bound of the speed, the height of the solitary wave is limited below that of the limiting solitary wave, while the height becomes smaller as the speed approaches the lower bound. Namely, a higher solitary wave propagates at higher speed. A solitary wave propagating at a speed close to the lower bound may be regarded as substantially the K–dV soliton. As far as generation of the K–dV soliton is concerned, incidentally, the Helmholtz resonators in the array may alternatively be replaced by acoustically compact, closed side branches of any shape, e.g. quarter-wavelength tube (Sugimoto 1995).

The previous experiments use a tube of length 7.4 m, to which the array of Helmholtz resonators is connected. The temporal pressure profile of the pulse and the propagation speed of the peak were measured experimentally and compared to the theory. This may be called a direct check on the assumption that the pulse has evolved into a solitary wave. Because of the good agreement with the theory, the existence of the acoustic solitary waves is proved. In the experiments, however, there remain technical points to be improved. One is the method of generating an initial pressure pulse in the tube. By discharging pressurized air stored in a high-pressure chamber through a small hole in a mechanical valve, it spreads spherically into the tube so that one-dimensional propagation is not established for a while. In consequence, a negative pressure (expansion) appears behind the main compression pulse. Because this pressure dent is propagated at a speed slower than the sound speed, it interfers with the subsonic solitary wave for a long time and makes measurements difficult. The other technical problem is the tube length, which is not long enough in comparison with the width of the solitary wave. In the present experiments, a new plane piston driver is constructed so that the initial pulse may become planar from the beginning, while the tube length is extended to 10.6 m. By using this tube with the same resonators connected, the previous results are first re-examined.

In addition to the direct check, the existence of the acoustic solitary wave is also shown by the following check. The solitary wave is the entity predicted by the steady-progressive-wave solutions to the lossless version of the nonlinear wave equations derived previously (Sugimoto 1992, 1996). In experiments, however, lossy effects due to boundary layers and jet loss at the throat of the resonator are more or less unavoidable, so that a perfect solitary wave cannot be achieved in reality. So the experiments are simulated numerically by solving the nonlinear wave equations including the weakly lossy effects to find how accurately the equations can describe the real evolution. Provided that the validity of the equations is proved, it will follow that the solitary wave can exist when the lossy effects are reduced. This check may be indirect but it is intrinsic. No other ways to prove the existence are available than recourse to this indirect check.

In what follows, the theory of the acoustic solitary wave is first summarized in § 2. After describing the experimental setup in § 3, characteristics of the resonator used are examined by measuring its acoustic admittance experimentally to compare it with the theory in § 4. Methods of the experiments are described in § 5 and a comparison of the pressure profile and propagation speed measured with the theory is given in § 6. This is merely a re-examination of the previous results. Experiments in a tube with

no array are made in parallel to highlight the effect of the array and to also verify the existing theory due to Chester (1964), Keller (1981) and Sugimoto (1991). In order to check validity of the equations, numerical simulations are carried out and compared with the experiments in § 7. Finally discussions are given to verify the existence of the acoustic solitary wave.

2. Summary of the theory of the acoustic solitary wave

2.1. *Nonlinear wave equations*

First, the theory of the acoustic solitary wave is summarized in this section. For the details, reference should be made to Sugimoto (1992, 1996). The same notation, apart from slight and obvious modifications, is used as in the references.

The solitary wave is characterized by two parameters. One is a size parameter of the array κ defined by

$$\kappa = \frac{V}{Ad} \ll 1, \tag{2.1}$$

which measures the magnitude of cavity volume V relative to tube volume Ad per axial spacing between neighbouring resonators, A and d being tube cross-sectional area and the axial spacing, respectively. The other is a natural angular frequency of the resonator, which is given, in the lossless case, as

$$\omega_0 = \sqrt{\frac{a_0^2 B}{L_e V}}, \tag{2.2}$$

where $a_0 (= \sqrt{\gamma p_0/\rho_0})$, B, and L_e denote, respectively, the linear sound speed, throat cross-sectional area and its length taking account of end corrections specified later, p_0 and ρ_0 being the pressure and the density of air in equilibrium, and γ the ratio of specific heats. Taking the magnitude of a typical acoustic Mach number ε measuring the order of nonlinearity and a typical angular frequency ω to be $\kappa/2$ and ω_0, respectively, the coupling parameter $K (= \kappa/2\varepsilon)$ and the tuning parameter $\Omega [= (\omega_0/\omega)^2]$ may be set equal to unity (Sugimoto 1992).

The existence of the solitary wave is predicted by the steady-progressive-wave solution to the lossless version of the following nonlinear wave equations. Introducing f and g to denote the excess pressure in the tube p' and in the cavity p'_c, respectively, by

$$\kappa f = \frac{(\gamma+1)}{\gamma}\frac{p'}{p_0} \quad \text{and} \quad \kappa g = \frac{(\gamma+1)}{\gamma}\frac{p'_c}{p_0}, \tag{2.3}$$

and defining the retarded time θ in a frame moving with the sound speed, and the far-field coordinate X, respectively, by

$$\theta = \omega_0\left(t - \frac{x}{a_0}\right) \quad \text{and} \quad X = \frac{\kappa\omega_0 x}{2a_0}, \tag{2.4}$$

t and x being the time and the axial coordinate along the tube, the nonlinear wave equations are given as follows (see (2.28)†, (2.29) and (A.4) in Sugimoto 1992):

$$\frac{\partial f}{\partial X} - f\frac{\partial f}{\partial \theta} = -\delta_R \frac{\partial^{1/2} f}{\partial \theta^{1/2}} - \frac{\partial g}{\partial \theta}, \tag{2.5}$$

† The coefficient κ in (2.28) should be corrected to K.

and

$$\frac{\partial^2 g}{\partial\theta^2} + \delta_r \frac{\partial^{3/2} g}{\partial\theta^{3/2}} + g = f + \tfrac{1}{2}\kappa N, \tag{2.6}$$

where the loss is brought about by hereditary effects due to the boundary layer on the tube wall and throat wall and is expressed in the form of the fractional derivative of 1/2-order, defined by

$$\frac{\partial^{1/2} f}{\partial\theta^{1/2}} = \frac{1}{\sqrt{\pi}} \int_{-\infty}^{\theta} \frac{1}{\sqrt{\theta - \theta'}} \frac{\partial}{\partial\theta'} f(X, \theta')\, \mathrm{d}\theta', \tag{2.7}$$

and the derivative of 3/2-order defined as that derived by differentiating the derivative of 1/2-order once with respect to θ. The loss due to the diffusivity of sound is negligible, i.e. the term with $\partial^2 f/\partial\theta^2$ has been dropped in (2.5), because the Reynolds number Re defined by $a_0^2/\nu\omega$, ν being the kinematic viscosity of air, is of order 10^7 in experiments to be described. Note that the boundary-layer effects introduce not only the loss (dissipation) but also dispersion. The parameters δ_R and δ_r are defined as

$$\delta_R = \frac{2C\sqrt{\nu/\omega_0}}{\kappa R^*} \quad \text{and} \quad \delta_r = \frac{2\sqrt{\nu/\omega_0}}{r^*}, \tag{2.8}$$

with $C = 1 + (\gamma - 1)/\sqrt{Pr}$, Pr being the Prandtl number, where R and r denote, respectively, the radius of the tube and of the throat, R^* and r^* being the reduced radii defined as $R/(1 - r^2/2dR)$ and r/c_L with $c_L = L'/L_e$. Here L_e $(= L + 2 \times 0.82r)$ accounts for the well-known end corrections at both ends of the throat and L' $(= L + 2r)$ for the viscous end corrections (Sugimoto 1992).

When the magnitude of pressure disturbances becomes high, it may be appropriate to include the nonlinear response of the resonator. It is taken into account through the term $\kappa N/2$ in (2.6) given by

$$N = \left(\frac{\gamma - 1}{\gamma + 1}\right) \frac{\partial^2 g^2}{\partial\theta^2} - \frac{2V}{(\gamma + 1)BL_e} \left|\frac{\partial g}{\partial\theta}\right| \frac{\partial g}{\partial\theta}, \tag{2.9}$$

where the first term on the right-hand side results from the nonlinearity due to the adiabatic process in the cavity, while the second term, derived semi-empirically, accounts for the jet loss resulting from difference in flow patterns on the inflow and outflow sides of the throat.

2.2. *Acoustic solitary wave*

The acoustic solitary wave is predicted by the steady-progressive-wave solution to (2.5) and (2.6) on neglect of all boundary-layer effects, i.e. δ_R and $\delta_r \to 0$, and the higher-order term $\kappa N/2$. Given a constant speed s in the (θ, X)-space, it is expressed in the form of the inverse function as (Sugimoto 1996)

$$-4\tan^{-1}\sqrt{\frac{f_+ - f}{f - f_-}} + \frac{2s}{\sqrt{-f_+ f_-}} \log\left|\frac{[\sqrt{-f_-(f_+ - f)} - \sqrt{f_+(f - f_-)}]^2}{(f_+ - f_-)f}\right| \equiv \mathscr{F}(f) = |\zeta|, \tag{2.10}$$

with $\zeta = \theta - sX + \text{constant}$ and $f_\pm$ given by

$$f_\pm = -2\left(s - \tfrac{2}{3}\right) \pm \sqrt{-\tfrac{4}{3}s + \tfrac{16}{9}}, \tag{2.11}$$

the signs $\pm$ ordered vertically, where s to limited to the range $0 < s < 1$, and $f_- < 0 < f_+$. With f given above, g is obtained as

$$g = \tfrac{1}{2}f^2 + sf. \tag{2.12}$$

The solution (2.10), which is valid for $0 < f \leqslant f_+$ over $-\infty < \zeta < +\infty$, gives a compression pulse having a peak value f_+ and symmetric form with respect to the peak. The peak value increases as s decreases from unity. But since $0 < s < 1$, f_+ is bounded below $8/3$ at $s = 0$. Thus the peak excess pressure of the solitary wave p'_p is in the range

$$0 < p'_p < \frac{8\kappa\gamma}{3(\gamma+1)}p_0. \tag{2.13}$$

The physical speed of propagation v is obtained by noting the definition of ζ as $v = a_0/(1 + \kappa s/2)$. Thus v is limited to the range

$$\frac{a_0}{1+\kappa/2} < v < a_0. \tag{2.14}$$

The propagation speed of the acoustic solitary wave is slower than the sound speed but faster than the threshold value $a_0/(1 + \kappa/2)$. The speed becomes faster as the height increases.

The solitary-wave solution for an arbitrary value of s as given by (2.10) is complicated. But it takes a simple form in the limiting cases as $s \to 0+$ and $s \to 1-$. In the former limit, the speed of propagation tends to the sound speed and the solution is given in the dimensional form for p' as

$$\frac{p'}{p_0} = \frac{8\kappa\gamma}{3(\gamma+1)}\cos^2\left[\frac{\omega_0}{4}\left(t - \frac{x}{a_0}\right)\right] \quad \text{for} \quad \left|\omega_0\left(t - \frac{x}{a_0}\right)\right| \leqslant 2\pi, \tag{2.15}$$

and $p'/p_0 \equiv 0$ for $|\omega_0(t - x/a_0)| > 2\pi$. Although (2.15) is the solution to (2.5) and (2.6), regularity is lost at both ends, i.e. the derivative of second order jumps there. In this sense, (2.15) is called a limiting solitary wave. As s tends to unity, on the other hand, f approaches the K–dV soliton. This is given dimensionally as

$$\frac{p'}{p_0} = \frac{\kappa\gamma\alpha}{(\gamma+1)}\mathrm{sech}^2\left[\sqrt{\frac{\alpha}{12}}\omega_0\left(t - \frac{x}{v}\right)\right], \tag{2.16}$$

with $\alpha = 3(1 - s)$ $(0 < \alpha \ll 1)$ and $v = a_0/[1 + \kappa(1 - \alpha/3)/2]$.

The acoustic solitary wave for an intermediate value of s is considerably different in waveform from the K–dV soliton. This may be found in a relation between a half-width and a peak value. The half-width of the solitary wave is defined as the interval $\Delta\zeta$ between two values of ζ at which f takes half of the peak value and is given by $2\mathscr{F}(f_+/2)$. As the peak value increases ($s \to 0+$), $\Delta\zeta$ does not change much but approaches 2π. As the peak value decreases ($s \to 1-$), of course, it diverges as the inverse square root of the height. This is one of the well-known properties of the K–dV soliton.

3. Experimental setup

The experimental setup is shown in figure 1 (see Hellemans 1999 and Sugimoto 2001 for photographs of the apparatus used in the previous experiment). It consists of a tube, a piston driver unit, and measuring instruments, which are described below.

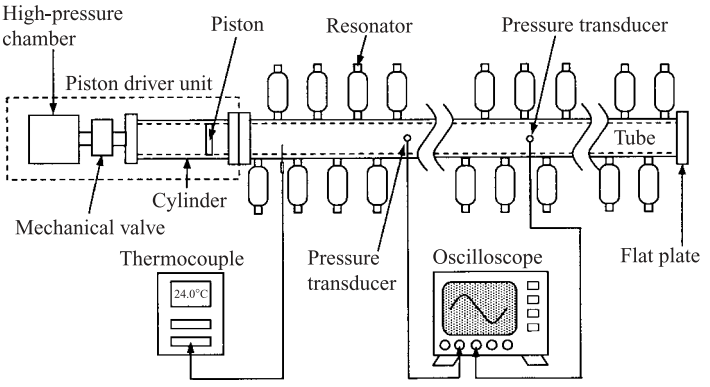

FIGURE 1. Experimental setup.

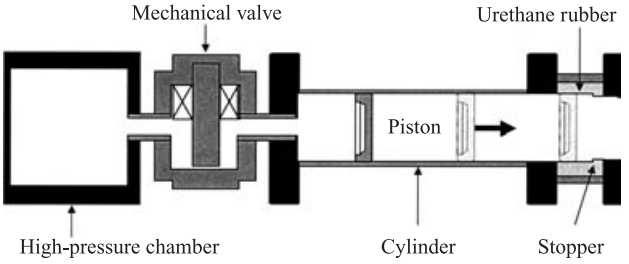

FIGURE 2. Cross-section of the piston driver unit to launch an initial pressure pulse where the pressurised air stored in the high-pressure chamber is released into the cylinder by opening the mechanical valve to accelerate the piston forward. The piston is decelerated to stop by the friction with the annular sheet of urethane rubber.

3.1. *Tube*

Two tubes are prepared, one with the array of resonators and the other without it. Both tubes are otherwise identical in geometry. Each tube is straight and of length 10.6 m, with circular cross-section of inner diameter $2R$ (=80 mm) and thickness 7.5 mm, and is made of stainless steel. The inner surface is polished very smoothly by honing with surface roughness R_z (ISO4287) below 0.6 μm. One end of the tube is closed by a flat plate while the other end is connected to the piston driver unit.

3.2. *Piston driver unit*

An initial pressure pulse is generated by driving a piston pneumatically in a cylinder. Figure 2 illustrates the assembly of the driver unit manufactured by Taiyo Limited, Osaka, Japan. It consists of a high-pressure chamber and a circular cylinder in which a piston is housed. A part of the cylinder on the opening side (to be connected to the tube) is lined with an annular sheet of urethane rubber whose inner surface is tapered slightly with a stopper in the form of a step. The high-pressure chamber and the cylinder are connected by a mechanical valve operated electromagnetically.

The volume of the high-pressure chamber is about 2×10^{-3} m^3 and the pressure stored in it is variable up to 0.5 MPa. The piston is of diameter 83 mm, of axial length 16 mm and of mass 0.163 kg, while the cylinder is of axial length 380 mm in total and the sheet is of axial length 73 mm and of inner diameter 80 mm at the step. The initial position of the piston can be varied in the cylinder. The final position at which the piston stops in the cylinder depends on the initial pressure stored in the high-pressure

FIGURE 3. Cross-section of the resonator cut by a plane including the axis.

chamber and the initial position of the piston. But the piston is blocked by the step of axial length 25 mm. No resonators can be connected along the cylinder of the driver unit.

3.3. *Resonators*

Resonators are the same as those used in the previous experiments and originally manufactured by Swagelok for the purpose of sample cylinders of gas (304L-HDF4-50 with suitable nipples). Each cylinder is of axisymmetric form and is made of stainless steel. The cross-section including the axis is depicted in figure 3. The resonator is of volume V ($=49.8\,\mathrm{cm}^3$) on average while the throat is of length L ($=35.6\,\mathrm{mm}$) and of diameter $2r$ ($=7.11\,\mathrm{mm}$) so that the volume of the throat is $1.41\,\mathrm{cm}^3$.

The resonators are connected to the tube in two arrays. As depicted in figure 1, they are along two lines (axial lines) on the cylindrical external surface of the tube, whose circumferential positions differ by 180° from each other. Further, the resonators are staggered in both arrays. In each array, the axial spacing between the centres of the throats of neighbouring resonators is 100 mm. In the upper array in figure 1, the axial distance between the right-hand tube end and the resonator nearest to it is chosen to be 25 mm so that the distance between the left-hand tube end and the resonator nearest to it becomes 75 mm. In the lower array, the above distances to the tube ends are reversed. There are 212 resonators connected, with the axial spacing d ($=50\,\mathrm{mm}$) in both arrays, and the size parameter κ takes the value 0.198. The reason for the staggered arrangement is to guarantee uniform axial spacing of the resonators in a mirror image at the closed end, and also to avoid unfavourable localized oscillations. As a reflected pressure wave is regarded as a mirror image of an incident wave, it is preferable to set the axial spacing uniform in a mirror image as well.

To connect the resonators to the tube, the wall is bored with piping thread NPT-1/4 in. Each resonator is screwed into the wall so that the end surface of the throat is flush with the inner surface of the tube. Ideally, all resonators should be identical. But they differ slightly from each other in shape and volume of the cavity, whereas the size of the throats may be regarded as being uniform in comparison with non-uniformity of the volume of the cavity. In order to avoid randomness in distribution, the resonators are arranged in order from the smallest one in volume and from the tube end on the driver side. Figure 4 shows the axial distribution of the resonators where the abscissa measures the distance from the tube end on the driver side and each volume includes error of $\pm 0.1\,\mathrm{cm}^3$ in measurements.

3.4. *Measuring instruments*

The temperature of the air in the tube and ambient pressure are measured by a thermocouple (Chino 1SCHS1-0K 01006132) and a barometer (not depicted in figure 1). The transient excess pressure due to a pulse is measured by two piezoelectric transducers (PCB Piezotronics HM113A26) with resolution 0.07 kPa and sensitivity $1.45 \pm 0.07\,\mathrm{mV\,kPa}^{-1}$ and a digital oscilloscope (LeCroy LT224). The transducers can be set at positions with axial spacing 0.4 m apart from the tube end on the driver side. For this purpose, the tube is bored with a NPT-1/4 in. array. In the tube with

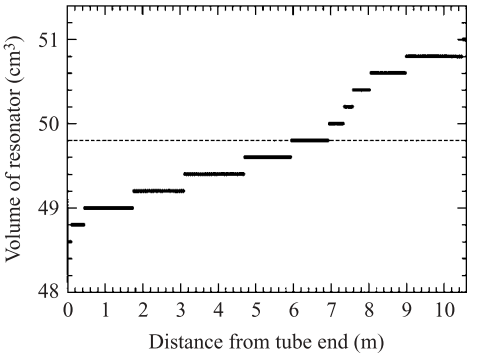

FIGURE 4. Distribution of the resonators along the tube.

the array of resonators, the circumferential positions of the holes differ in angle by 90° from those of resonators. Each transducer is connected with its face flush with the inner surface of the tube. Holes not in use are plugged by nipples to avoid leakage. When the pressure in the cavity is measured, the transducer is connected to the bottom of the resonator by removing the end nipple.

4. Linear characteristics of the resonator

4.1. *Acoustic admittance of the resonator*

Before embarking on experiments, the validity of the linearized version of (2.6) is checked by measuring an acoustic admittance (or acoustic mobility) of the resonator experimentally. The relevance of the hereditary term is especially important. To this end, it is appropriate to put (2.6) into dimensional form as (see (A.4) in Sugimoto 1992)

$$\frac{\partial^2 p_c'}{\partial t^2} + \frac{2\sqrt{\nu}}{r^*}\frac{\partial^{3/2} p_c'}{\partial t^{3/2}} + \omega_0^2 p_c' = \omega_0^2 p' + \frac{\gamma - 1}{2\gamma p_0}\frac{\partial^2 p_c'^2}{\partial t^2} - \frac{V}{\rho_0 a_0^2 B L_e}\left|\frac{\partial p_c'}{\partial t}\right|\frac{\partial p_c'}{\partial t}. \tag{4.1}$$

Ignoring the nonlinear terms, suppose the excess pressure at the entrance of the throat and the velocity of air flowing into the throat be in the form of $p' = \mathrm{Re}\{P\exp(\mathrm{i}\omega t)\}$ and $w = \mathrm{Re}\{W\exp(\mathrm{i}\omega t)\}$, respectively, where P and W denote respective complex amplitudes, and ω (>0) in this section is an angular frequency, not a typical frequency as used in § 2. The acoustic admittance of the resonator is defined as BW/P. Noting that the conservation of mass in the cavity requires

$$\rho_0 B w = \frac{V}{a_0^2}\frac{\partial p_c'}{\partial t}, \tag{4.2}$$

and using (4.1), the dimensionless acoustic admittance Y is defined in reference to the typical admittance $A/\rho_0 a_0$ of the tube as follows:

$$Y(\omega) = \frac{\rho_0 a_0}{A}\frac{BW}{P} = \frac{B}{A}\frac{a_0}{L_e}\left(\frac{\mathrm{i}\omega}{\omega_0^2 - \omega^2 - \sqrt{2\nu\omega^3}/r^* + \mathrm{i}\sqrt{2\nu\omega^3}/r^*}\right). \tag{4.3}$$

Note that the 1/2- and 3/2-order derivatives of $\exp(\mathrm{i}\omega t)$ are given, respectively, by $[(1+\mathrm{i})/\sqrt{2}]\omega^{1/2}\exp(\mathrm{i}\omega t)$ $[=(\mathrm{i}\omega)^{1/2}\exp(\mathrm{i}\omega t)]$ and $[(-1+\mathrm{i})/\sqrt{2}]\omega^{3/2}\exp(\mathrm{i}\omega t)$ $[=(\mathrm{i}\omega)^{3/2}\exp(\mathrm{i}\omega t)]$.

As Y becomes purely imaginary in the limit as $\nu \to 0$, the real part of Y is due to the loss. It takes the maximal value

$$\mathrm{Re}\{Y\}_{\max} = \frac{B}{A}\frac{a_0}{L_e}\frac{r^*}{\sqrt{2\nu\omega_0}} = \frac{Ba_0}{2AL_e\Delta\omega} \quad \text{at} \quad \omega = \omega_m = \omega_0 - \Delta\omega, \tag{4.4}$$

with a frequency downshift $\Delta\omega$ given by

$$\Delta\omega = \frac{\sqrt{\nu\omega_0}}{\sqrt{2}r^*} = \frac{\delta_r}{\sqrt{8}}\omega_0, \tag{4.5}$$

where $\Delta\omega$ is truncated at the first order of δ_r. Similarly, the imaginary part of Y takes the maximal value

$$\mathrm{Im}\{Y\}_{\max} = \frac{B}{A}\frac{a_0}{L_e}\frac{r^*}{\sqrt{8\nu\omega_0}} = \frac{Ba_0}{4AL_e\Delta\omega} \quad \text{at} \quad \omega = \omega_- = \omega_0 - 2\Delta\omega, \tag{4.6}$$

and the minimal value

$$\mathrm{Im}\{Y\}_{\min} = -\frac{B}{A}\frac{a_0}{L_e}\frac{r^*}{\sqrt{8\nu\omega_0}} = -\frac{Ba_0}{4AL_e\Delta\omega} \quad \text{at} \quad \omega = \omega_+ = \omega_0. \tag{4.7}$$

Note that the maximal value of the real part is just double of that of the imaginary part and the imaginary part takes its minimum at ω_0 to the first order of δ_r.

4.2. *Measurements of the acoustic admittance*

The acoustic admittance is measured experimentally by using a long tube with a single resonator connected. Launching plane pressure waves from the far end of the tube toward the resonator, incident waves on the resonator and reflected waves from it are calculated from the pressure measured at four points at least. Taking the axial coordinate z along the tube with its origin at the resonator, let the excess pressure and the axial velocity of air in the region $z < 0$ be denoted by p'_- and u_-, respectively and given as follows:

$$p'_- = I_- \exp[\mathrm{i}\omega(t - z/a_0)] + R_- \exp[\mathrm{i}\omega(t + z/a_0)], \tag{4.8a}$$

$$u_- = (\rho_0 a_0)^{-1}\left\{I_- \exp[\mathrm{i}\omega(t - z/a_0)] - R_- \exp[\mathrm{i}\omega(t + z/a_0)]\right\}, \tag{4.8b}$$

and let the excess pressure p'_+ and the axial velocity u_+ in $z > 0$ be given as follows:

$$p'_+ = I_+ \exp[\mathrm{i}\omega(t + z/a_0)] + R_+ \exp[\mathrm{i}\omega(t - z/a_0)], \tag{4.9a}$$

$$u_+ = (\rho_0 a_0)^{-1}\left\{-I_+ \exp[\mathrm{i}\omega(t + z/a_0)] + R_+ \exp[\mathrm{i}\omega(t - z/a_0)]\right\}, \tag{4.9b}$$

where $I_\pm$ and $R_\pm$ are the complex amplitudes of the incident and reflected waves, and the real parts are taken on the respective right-hand sides. Continuity of the pressure and the mass flux at $z = 0$ requires

$$I_- + R_- = I_+ + R_+ = P, \tag{4.10a}$$

$$\frac{S}{\rho_0 a_0}(I_- - R_-) = \frac{S}{\rho_0 a_0}(-I_+ + R_+) + BW, \tag{4.10b}$$

where S denotes the cross-sectional area of the tube used for measurements of the acoustic admittance and the value of S used is not equal to that of A described in § 3. Eliminating BW by using $(A/\rho_0 a_0)YP$, Y is calculated by

$$Y = \frac{2S}{A}\left(\frac{I_- - R_+}{I_+ + R_+}\right). \tag{4.11}$$

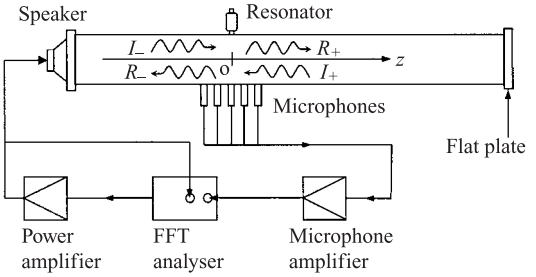

FIGURE 5. Experimental setup for measurements of the acoustic admittance of the resonator where the z-axis is taken along the tube with its origin at the resonator in the sense toward the flat plate, and the complex amplitudes of the incident waves on the resonator and the reflected ones from it are designated by $I_\pm$ and $R_\pm$, respectively.

The measurements are made by using a thin tube of inner diameter 40 mm and of length 5 m, which is made of stainless steel and of thickness 5 mm. The experimental setup is shown in figure 5. A single resonator is connected at a point 2 m away from one end of the tube where the speaker (Fostex FE87) is mounted, while the other end is closed by a flat plate. The speaker is located at $z = -2$ m and the flat plate at $z = 3$ m. The pressure is measured at five points: $z = 0$ m, ± 0.1 m and ± 0.2 m where the centres of the microphone (Aco Type 7016) are positioned. The measurements of the pressure are undertaken by Ono Sokki Inc., Yokohama, Japan. From the pressures measured at two points at $z < 0$ and two points at $z > 0$, the left- and right-going waves are calculated to yield $I_\pm$ and $R_\pm$, and then Y is evaluated by (4.11). The loss in the tube may be negligibly small because the distance between the measuring points is short.

Taking the typical acoustic admittance $A/\rho_0 a_0$ as that in the tube of diameter 80 mm ($S/A = 1/4$), figure 6 shows the real and imaginary parts of Y where the solid circles represent the data measured at temperature 18.8 °C and atmospheric pressure 0.1016 MPa, and the solid lines represent the theoretical values. The sound pressure level is kept in a range between 95 and 85 dB for all frequencies except for low ones less than 50 Hz, and the resolution in frequency is 1 Hz. The theoretical curves are drawn by calculating (4.3) numerically with the material constants: $a_0 = 343.0\,\mathrm{m\,s^{-1}}$ and $\nu = 0.1491 \times 10^{-4}\,\mathrm{m^2\,s^{-1}}$ (see the Appendix), so that $\omega_0/2\pi = 239.5$ Hz, $\delta_r = 5.773 \times 10^{-2}$ and $\Delta\omega/2\pi = 4.888$ Hz. The measured data appear to fit with the theory very well except for frequencies near the extrema. Scattered data at low frequencies are obviously due to noise in the measurements. At the frequency where the imaginary part vanishes and the real part takes its maximum, the axial velocity is in phase with the pressure fluctuation. Then the magnitude of the admittance becomes comparable with that in the tube in spite of the fact that the cross-sectional area of the throat is merely 1% of that of the tube.

Table 1 compares quantitatively the measured values with the thoretical ones given by (4.3) and the asymptotic ones given by (4.4) to (4.7). The frequencies for the extrema are found to agree with the theoretical values very well. But the extremal values are smaller than the theoretical ones in magnitude. This discrepancy of order 10% may be attributed to the nonlinear effects, especially due to the jet loss at the throat. The acoustic Mach number in the throat $|w|/a_0$ is estimated as $|W|/a_0 = (AY/\gamma B)|P|/p_0$. Since A/B is of order 10^2 and $|P|/p_0$ is of order 10^{-5} for 95 dB in SPL, the maximum acoustic Mach number attains the order 10^{-3} when $|Y|$ becomes of order unity in the vicinity of ω_m. In (4.1), the jet loss term is estimated in comparison with that of the

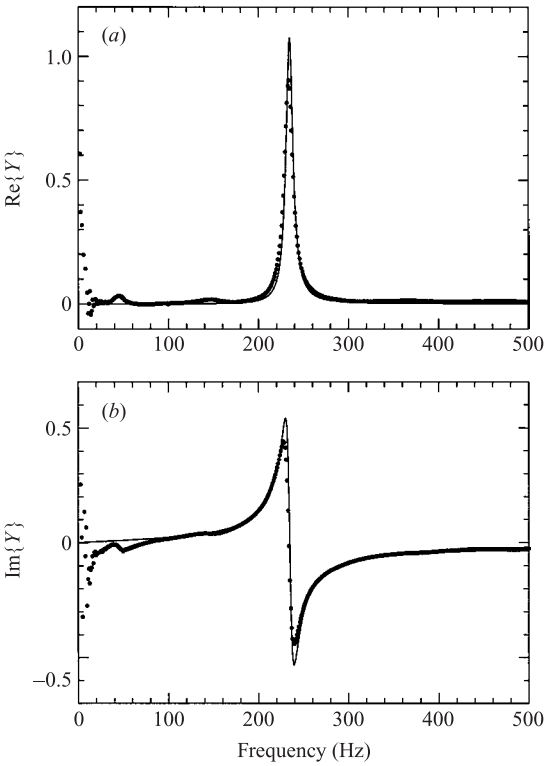

FIGURE 6. Real and imaginary parts of the dimensionless acoustic admittance Y of the resonator to be used in the array where the solid circles indicate the measured data at temperature 18.8 °C and atmospheric pressure 0.1016 MPa, and the solid lines represent the theoretical values calculated by (4.3).

	$\omega_-/2\pi$ (Hz)	$\mathrm{Im}\{Y\}_{\max}$	$\omega_m/2\pi$ (Hz)	$\mathrm{Re}\{Y\}_{\max}$	$\omega_+/2\pi$ (Hz)	$\mathrm{Im}\{Y\}_{\min}$
Measured values	228	0.440	234	0.902	240	−0.441
Theoretical values	230.0	0.543	234.6	1.075	239.4	−0.532
Asymptotic values	229.7	0.532	234.6	1.065	239.5	−0.532

TABLE 1. Quantitative comparison of the extremal values of the acoustic admittance Y at temperature 18.8 °C and atmospheric pressure 0.1016 MPa.

linear loss by taking the ratio as follows:

$$\left(\frac{2\sqrt{\nu}}{r^*}\frac{\partial^{3/2}p_c'}{\partial t^{3/2}}\right)^{-1}\left(\frac{V}{\rho_0 a_0^2 B L_e}\left|\frac{\partial p_c'}{\partial t}\right|\frac{\partial p_c'}{\partial t}\right)=\left(\frac{2\sqrt{\nu}L_e}{r^*}\frac{\partial^{1/2}w}{\partial t^{1/2}}\right)^{-1}|w|w\sim\left(\frac{a_0 r^*}{2\sqrt{\nu\omega}L_e}\right)\frac{|W|}{a_0}, \tag{4.12}$$

where (4.2) has been used. In the vicinity of ω_m, the factor within the parentheses in the last term is $AY/\sqrt{2}B$ by (4.4). Thus the ratio is estimated to be $(1/\sqrt{2}\gamma)(A/B)^2|Y|^2|P|/p_0$ and is found to be of order 10^{-1}. Since the jet loss enhances the linear loss, it is conjectured that the maximal value of the real part of Y measured

is smaller than the theoretical value by about 10%. This will be true for the imaginary parts as well. But it is revealed that the linearized version of (2.6) can give an adequate description of the response of the resonator for frequencies away from ω_m.

Finally the following point is noted. In the expression for ω_0 ($=\sqrt{a_0^2 B/L_e V}$), V is taken as the volume of the cavity, which is slightly different from the volume of the resonator because it excludes the throat. In fact, the value 49.8 cm^3 used so far is the volume of the resonator including 1.41 cm^3 for the throat. Although this difference is usually negligible, it turns out that ω_0 based on the volume of the resonator agrees better with the experimental value than that based on the volume of the cavity. Therefore (4.2) may rather be interpreted as the equation for the conservation of mass for the whole resonator. In the following, hence, ω_0 is defined using the volume of the resonator.

5. Experiments

5.1. *Procedures for the experiments*

Procedures for the experiments are described briefly. With the piston set at an appropriate position in the cylinder, the tube and the piston driver unit are connected through flanges. It is important to keep the air column confined hermetically. The temperature of the air column and ambient pressure are measured and taken as the equilibrium temperature T_0 and pressure p_0, respectively. Storing the pressurized air in the high-pressure chamber and releasing it by opening the valve, the piston is accelerated in the cylinder and decelerated to stop by friction between the piston and the urethane sheet. By this movement, the pressure pulse is generated in the air column. It continues to propagate back and forth, subjected to many reflections at the flat plate and the piston surface, until it decays away eventually. The piston is caught by the sheet so tightly that no air leaks through the gap between the piston and the sheet.

In the following, let the x-axis be taken along the tube and directed toward the flat plate with its origin at the contact surface of the two flanges on the tube side and on the driver side. Let the initial and final positions of the piston surface be at $x = x_S$ and $x = x_P$ ($x_S < x_P < 0$), respectively. The air column finally occupies the region $x_P < x < x_E$ where x_E (=10.6 m) denotes the coordinate of the surface of the flat plate at the closed end. The axial length of the column is denoted by l ($=x_E - x_P$), and is longer than the tube length.

The pressure in the air column is measured at two positions, usually $x = 0.4$ m and 5.2 m, respectively. The former position is used to measure a pressure pulse propagating down the tube initially when the piston is driven. This pulse is called the initial pulse. The latter position is used to measure pulses reflected and propagating unidirectionally. At this position, reflected pulses propagating toward the flat plate or the piston can be identified easily. The pressure in the cavity of the resonator is measured at a position $x = 0.425$ m or $x = 5.225$ m, slightly different from the above positions.

5.2. *Initial pressure pulse*

Figures 7(a) and 7(b) show the profiles of the initial pressure pulses measured at $x = 0.4$ m in the tube with and without the array of resonators, respectively, as jagged lines, where the origin of the time is adjusted to the maximum in the pressure and the experimental conditions are: $T_0 = 25.0\,^\circ$C and $p_0 = 0.1007$ MPa for (a) and $T_0 = 24.8\,^\circ$C and $p_0 = 0.1010$ MPa for (b). The meaning of the smooth lines will be

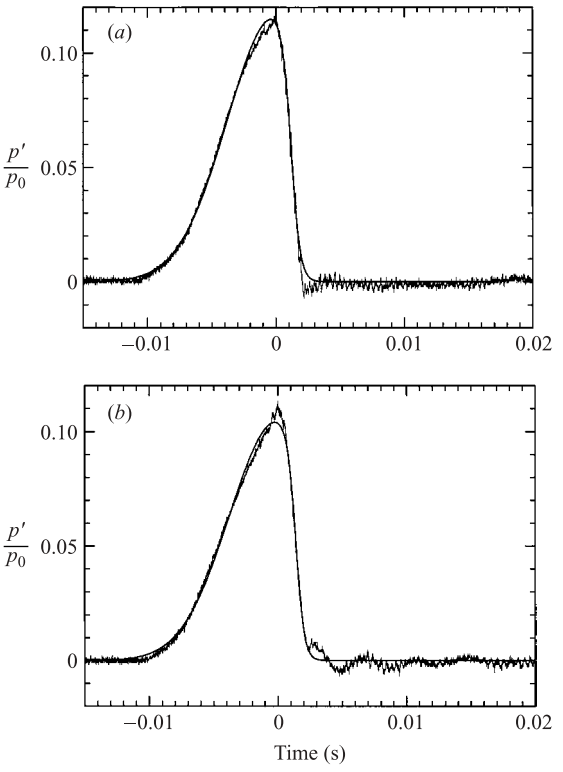

FIGURE 7. Temporal profiles of the excess pressure measured at the position $x = 0.4\,\mathrm{m}$ where (*a*) shows the profiles in the tube with no array of resonators at $T_0 = 25.0\,^{\circ}\mathrm{C}$ and $p_0 = 0.1007\,\mathrm{MPa}$ and (*b*) those in the tube with the array at $T_0 = 24.8\,^{\circ}\mathrm{C}$ and $p_0 = 0.1010\,\mathrm{MPa}$ respectively. The smooth lines represent the profiles fitted by the function (7.2) with the coefficients given in table 2.

explained later. The data shown here and hereafter are sampled at 10 μs and are raw in the sense that no filtering has been applied. Some noise is observed when the piston skids on the urethane rubber. The profiles are of asymmetric form, steepened backward (rightward) with respect to the peak. In figure 7(*a*), the excess pressure increases from zero to attain a peak and decreases to zero without any tail. It consists of the compression phase only. Unlike in the previous experiments using the mechanical valve, no negative pressure is generated behind the main pulse. The profile in (*b*) is slightly different from the one in (*a*) because it has already been influenced by eight resonators in $0 < x < 0.4\,\mathrm{m}$. A small oscillatory tail behind the main pulse (apart from the noise) is caused by dispersion due to the resonators.

These profiles are obtained when the initial pressure in the high-pressure chamber, denoted by p_H, and the initial position of the piston x_S are set at 0.2 MPa and −0.21 m, respectively, while the final position x_P is located at −0.054 m. If p_H and x_S are held constant, the pressure profiles are reproduced with high accuracy in the respective tubes. In passing, the profile in (*a*) enables us to guess the motion of the piston. Since the excess pressure is proportional, in the linear theory, to the piston velocity, it is considered that the piston is accelerated gradually but decelerated very rapidly to stop without any bounce. The area under the profile corresponds to the total displacement of the piston.

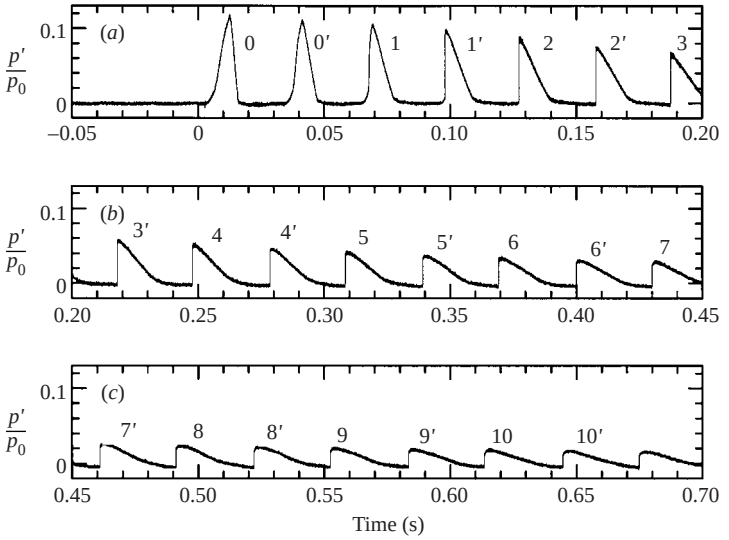

FIGURE 8. Temporal profile of the excess pressure p'/p_0 measured at $x = 5.2$ m in the tube with no array of resonators and at $T_0 = 25.0\,^{\circ}$C and $p_0 = 0.1007$ Mpa. The pulses labelled n ($n = 0, 1, 2, \ldots, 10$) denote those which have so far undergone reflection n-times at the piston and are propagating toward the flat plate, while the pulses labelled n' ($n = 0, 1, 2, \ldots, 10$) have also undergone reflection n-times but they are propagating toward the piston, the origin of time being set at the peak in figure 7(a).

5.3. *Experiments in the tube with no array*

For the initial pulse in figure 7(a), figure 8 shows the profile measured at $x = 5.2$ m. The initial pulse and its reflections by the flat plate and the piston are recorded with respective time delays. The pulses labelled n ($n = 0, 1, 2, \ldots, 10$) are the ones which have returned to the position at $x = 5.2$ m after being reflected n-times by the piston (or reflected n-times by the flat plate) and are propagating toward the flat plate. The pulses labelled n' ($n = 0, 1, 2, \ldots, 10$) are subjected to reflection by the piston n-times (or reflected $(n + 1)$-times by the flat plate) and propagating toward the piston. The pulse labelled n has travelled the distance $2nl$ since it initially passed the position at $x = 5.2$ m.

The lifetime of the pulse may be seen in this figure. The initial smooth pulse in figure 7(a) steepens forward to evolve into a triangular pulse with a shock ahead. This is a well-known nonlinear process. Once the shock is formed, the shock strength, i.e. the magnitude of discontinuity, is increased rapidly but gradually decreased while the width of the pulse is increased. As the shock strength become small, the boundary-layer effects dominate so that the upper edge of the shock tends to be rounded and a tail tends to emerge, deviating from the exact triangular shape (Sugimoto 1991). Since the tube length is limited, the tail and the next reflected pulse overlap so that the tail is not seen clearly. Eventually the pulse decays to enter a linear regime as it becomes old. Thus the shock appears unless the array of resonators is connected. This experiment has another purpose: to examine validity of (2.5) without the term of $\partial g/\partial\theta$ for evolutions in the tube with no array. This is checked by numerical simulations in § 7.

5.4. *Experiments in the tube with the array*

When the array of resonators is connected, the features of propagation are dramatically changed. Figure 9 shows the profile measured at $x = 5.2$ m. The pulses

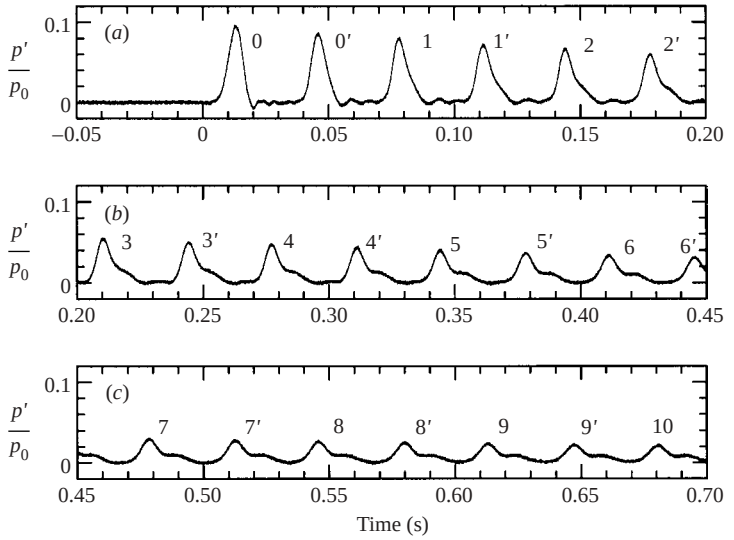

FIGURE 9. Temporal profile of the excess pressure p'/p_0 measured at $x = 5.2\,\mathrm{m}$ in the tube with the array of resonators and at $T_0 = 24.8\,^{\circ}\mathrm{C}$ and $p_0 = 0.1010\,\mathrm{MPa}$. The pulses labelled n ($n = 0, 1, 2, \ldots, 10$) denote those which have so far undergone reflection n-times at the piston and are propagating toward the flat plate, while the pulses labelled n' ($n = 0, 1, 2, \ldots, 9$) have also undergone reflection n-times but they are propagating toward the piston, the origin of time being set at the peak in figure 7(b).

are labelled in the same way as in figure 8. The pulse never evolves into a shock and remains smooth in profile. At the early stage, an oscillatory tail appears behind the main pulse. But it disappears in the course of propagation and the pulse tends to take a symmetric form, though a small hump tends to emerge behind the main pulse. Once such a profile is attained, it persists, which is one of the main features of solitary waves. But the peak pressure tends to decrease in the course of propagation, whereas the pulse width does not appear to change significantly.

In order to generate an initial pulse of higher peak with its width fixed, it is necessary not only to set p_{H} higher but also to set the piston further back, i.e. take $|x_{\mathrm{S}}|$ longer. By setting p_{H} to 0.3, 0.4 and 0.5 MPa with x_{S} at -0.25, -0.29 and $-0.33\,\mathrm{m}$, respectively, the experiments are carried out. These combinations make the peak pressure higher but keep the width almost constant. In all cases, it turns out that the evolution is the same qualitatively.

6. Results of the experiments

In the tube with the array of resonators, it is seen that shock formation is suppressed and the initial pulse remains smooth in profile. Although a perfect solitary wave would not be expected in reality, it is interesting to examine whether or not such smooth pulses possess the properties of an acoustic solitary wave. In this section, the profiles and the propagation speeds are checked against the theory.

6.1. *Comparison of the profiles*

The solitary wave is determined uniquely in terms of s alone. Measuring the peak pressure p'_p in the profile, s is calculated by (2.3) and (2.11) as

$$s = \tfrac{1}{2}\bigl(1 - f_+ + \sqrt{1 + \tfrac{2}{3} f_+}\bigr) \quad \text{with} \quad f_+ = \frac{(\gamma + 1)}{\kappa\gamma}\frac{p'_p}{p_0}, \tag{6.1}$$

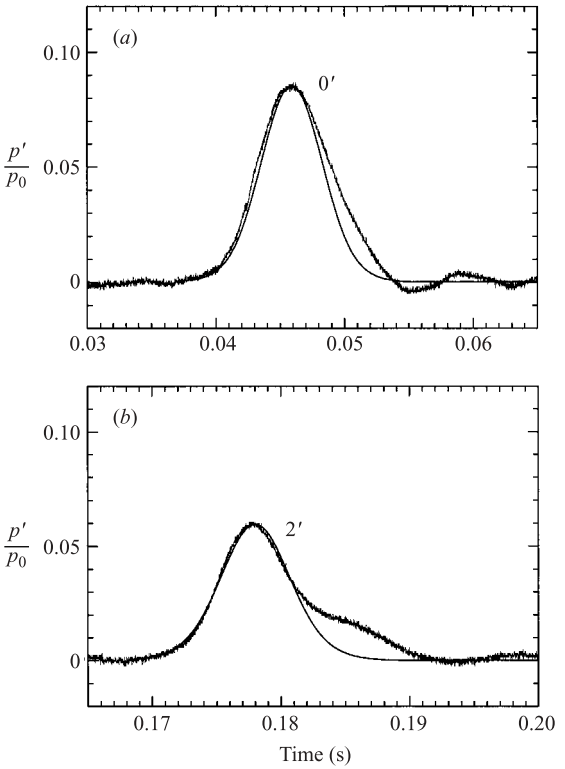

FIGURE 10. Comparison of the temporal profiles of the measured pulses in figure 9 with those of the solitary wave where the jagged lines in (*a*) and (*b*) represent, respectively, the profiles of the pulse labelled 0′ and 2′, with the theoretical ones with the corresponding peak values as smooth lines.

where $\kappa = 0.198$ and $\gamma = 1.402$ (see the Appendix). For the pulses labelled 0′ and 2′ in figure 9, the respective profiles of the solitary waves versus the dimensional time are drawn as thin lines in figure 10(*a*) and figure 10(*b*) where the experimental profiles are indicated by the thick lines and the theoretical ones are translated horizontally so that both peaks coincide. It is found that the measured profile in figure 10(*a*) fits well with the theoretical one overall, while the profiles in figure 10(*b*) agree very well except for the tail and hump. It will be revealed later that the tail and hump are caused by the boundary layers and jet loss, respectively.

For other pulses, a similar check needs a lot of space, so instead a relation between a half-width in time and a peak pressure is sought. The half-width is defined as a time interval between two instants at which p' takes half the value of the peak. To obtain it from the data measured, the maximum is first identified and then the instants of its half-value are sought after the profile has been smoothed by averaging five consecutive data points. Denoting the half-width by $1/\omega_h$, figure 11 depicts the relation between the dimensionless half-width ω_0/ω_h and the peak pressure p'_p relative to p_0 for the pulses labelled 0, 1, 2, ... in figure 9. Here the open symbols indicate the data measured when the initial pressure in the high-pressure chamber is set at 0.2, 0.3, 0.4, and 0.5 MPa. The solid symbols indicate the initial values of the peak pressure and the half-width measured at $x = 0.4$ m. The initial half-width is almost constant versus p'_p/p_0 because the initial position of the piston is set to guarantee this.

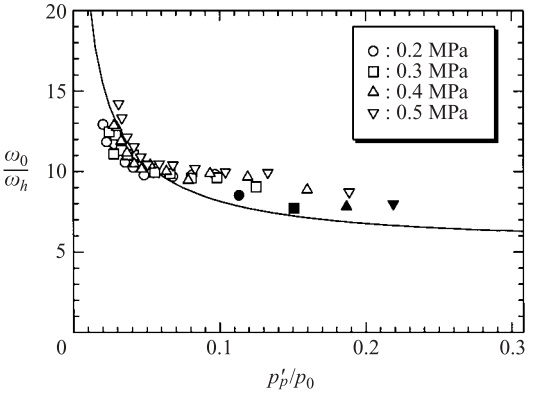

FIGURE 11. Relation between the dimensionless half-width ω_0/ω_h and the peak pressure p'_p/p_0 for the pulses labelled 0, 1, 2, ... in figure 9 where the open symbols indicate the measured data for the initial pressure in the high-pressure chamber set at 0.2, 0.3, 0.4 and 0.5 MPa, while the solid symbols indicate, respectively, the peak pressure and half-width of the initial pulses observed at $x = 0.4$ m, and the solid line represent the theoretical relation for the solitary wave.

For $\kappa = 0.198$, the peak pressure should be below $0.308\,p_0$ for the limiting solitary wave. The solid line represents the theoretical value of ω_0/ω_h $[=\Delta\zeta = 2\mathscr{F}(f_+/2)]$ calculated by (2.10). Since the peak pressure decreases in the course of propagation, the data indicated by the same symbol move leftward as the label n ($n = 0, 1, 2, \ldots$) is increased. The initial profiles are obviously different from those of the solitary waves, whereas all initial values are close to the theoretical curve, but they first depart from the theoretical curve and then approach it again. Thus it may be said that the measured data agree well with the theory as p'_p/p_0 becomes smaller. The relation of the inverse square of the peak pressure is seen to be satisfied. But as the peak pressure becomes large, there is a discrepancy, which will turn out to be attributed to the jet loss.

6.2. *Comparison of the propagation speeds*

Next the propagation speed is checked. The speed is calculated by measuring the elapsed time for which the pulse travels a certain distance, and then dividing the distance with the time. For this purpose, new measurements are taken at two positions $x = 6$ m and $x = 6.8$ m. These positions are chosen in view of the distribution of resonators in figure 4. The resonators in $6\,\text{m} < x < 6.8\,\text{m}$ are uniformly distributed and have volume equal to the mean value $49.8\,\text{cm}^3$. The speed is calculated by following the method used in measuring the half-width. Identifying two instants when the pressure takes half the value of the peak, the mid-time between them is sought for each pulse measured at $x = 6$ m and $x = 6.8$ m. Thus the elapsed time for two mid-times is obtained so that the propagation speed is calculated by dividing the distance 0.8 m with this time.

Since the propagation speed v is close to the sound speed, deviation from it is important. For the solitary wave, v is given by $a_0/(1 + \kappa s/2)$, and fraction $(a_0 - v)/a_0$ is expressed in terms of s given by (6.1) as

$$\frac{a_0 - v}{a_0} = \frac{\kappa s}{2 + \kappa s}. \tag{6.2}$$

Figure 12 shows the relation between the fraction $(a_0 - v)/a_0$ and the peak pressure p'_p/p_0 where the measured data are marked by the symbols and the theoretical

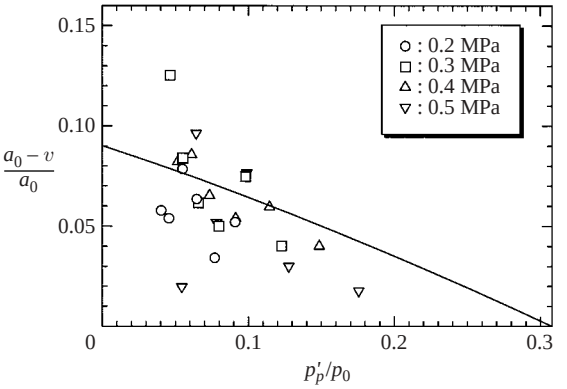

FIGURE 12. Relation between the fraction $(a_0 - v)/a_0$ and the peak pressure p'_p/p_0 calculated from the pulses measured at $x = 6$ m and $x = 6.8$ m where the symbols indicate the data measured for initial pressure in the high-pressure chamber set at 0.2, 0.3, 0.4 and 0.5 MPa, and the solid line represents the theoretical relation for the acoustic solitary wave.

relation (6.2) with (6.1) is indicated in the solid line. The symbols designate the data measured for the cases where the initial pressure in the high-pressure chamber is set at 0.2, 0.3, 0.4, and 0.5 MPa. In each case, the pressure profiles measured at $x = 6$ m and 6.8 m are displayed in the same way as in figure 9 and the pulses are labelled, though not reproduced here. The speed is calculated by taking the pulses labelled from 0 to 5.

This is because reflection by the flat plate makes the measurements difficult as the peak pressure becomes smaller and the pulse width becomes wider. In figure 12, the data scatter around the solid line. Since the fraction is a first-order quantity in κ, it contains an error of κ^2, i.e. about 4% in the present case. Further, a non-uniformity of a few percent exists in distribution of the resonators shown in figure 4. But the data for 0.3 and 0.4 MPa agree with the theory relatively well.

7. Results of the numerical simulations

The comparison in the preceding section reconfirms the existence of the acoustic solitary wave to the same extent as in the previous work (Sugimoto *et al.* 1999). In experiments, however, effects of the boundary layers and jet loss always mask the ideal, lossless evolution. To establish existence of the solitary wave, nevertheless, the validity of (2.5) and (2.6) must be checked against experiments. In this section, the evolution of the initial pulse is simulated numerically by taking account of the boundary layers and the jet loss. This check clarifies how accurately (2.5) and (2.6) can describe real evolution. If they turn out to be reliable enough, then it can be concluded that the acoustic solitary wave exists when the boundary-layer effects and the jet loss are suppressed.

However another problem arises. The equations assume a tube of semi-infinite length whereas the actual tube length is limited. So it may be considered that bi-directional propagation should be solved in the bounded region. Even so, however, it is worthwhile to solve (2.5) and (2.6) by regarding the distance in uni-directional propagation as that over which the pulse has actually travelled in the tube subject to reflection. This result is expected to be applicable because the propagation of a single pulse is considered and reflection at both ends will yield only a small phase shift in

view of the analytical results on collision of shocks (Tatsumi & Tokunaga 1974) or solitons (Oikawa & Yajima 1973).

7.1. *Initial conditions and parameter values*

The initial-value problem of (2.5) and (2.6) is posed for $X > 0$ with an initial condition for f given by

$$f(\theta, X = 0) = F(\theta) \quad (-\infty < \theta < \infty), \tag{7.1}$$

where $F(\theta)$ takes a pulse form with its peak at $\theta = 0$ by making use of the arbitrariness of additive constants in the definitions of θ and X on the right-hand sides of (2.4), i.e. $\theta = \omega_0[t-(x-x_1)/a_0]$ and $X = \kappa\omega_0(x-x_1)/2a_0$, x_1 being a constant. Note that an initial condition for g is not prescribed independently of F but given by a solution of (2.6) with $f = F(\theta)$. A functional form of F is given by fitting the pressure profile in figure 7 with an appropriate function.

Supposing that the profiles may be a Gaussian distorted on its right-hand side, though there are no physical reasons behind assuming this, they are fitted by the following function:

$$\frac{p'}{p_0} = \frac{p'_p}{p_0}\left\{\frac{1+\tanh[c_1(t_o-t)]}{1+\tanh(c_1 t_o)}\right\}\exp(-c_2 t^2), \tag{7.2}$$

where c_1, c_2 and t_o are dimensional quantities to be determined. The factor in the curly brackets is responsible for the distortion from the Gaussian $\exp(-c_2t^2)$. The initial condition F is then given by making use of (2.3) and replacing t with θ/ω_0 at $x = x_I = 0.4$ m as follows:

$$F(\theta) = \tfrac{1}{2}\mathscr{A}\{1+\tanh[\alpha_1(\theta_o-\theta)]\}\exp(-\alpha_2\theta^2), \tag{7.3}$$

with

$$\mathscr{A} = \frac{(\gamma+1)}{\kappa\gamma}\frac{p'_p}{p_0}\left[\frac{2}{1+\tanh(c_1 t_o)}\right], \tag{7.4}$$

$\alpha_1 = c_1/\omega_0$, $\alpha_2 = c_2/\omega_0^2$ and $\theta_o = \omega_0 t_o$.

Here the technical method of fitting the profile is briefly mentioned. Because the measured data are scattered due to noise and deficiency in resolution, the maximum pressure at $t = 0$ is not taken as p'_p immediately but is evaluated as follows. Since the profile on the left-hand side of the peak is expected to be the Gaussian, two factors $p'_p/p_0[1+\tanh(c_1t_o)]$ and c_2 are evaluated by using the least-squares method to fit the data in the range $t < 0$ and $0.1p'_p \leqslant p' \leqslant p'_p$ where p'_p is chosen temporarily to be the maximum value at $t = 0$ and $\tanh[c_1(t_o-t)]$ is approximated to be unity. With these factors available, then, c_1 and t_o are also determined by the least-squares method for the data for $t > 0$ and $0.1p'_p \leqslant p' \leqslant 0.9p'_p$. Thus p'_p/p_0 and c_1 are obtainable. On making a fit for $t \leqslant 0$, the factor $\tanh[c_1(t_o-t)]$ has been set equal to unity. The validity of this is endorsed now by the values of c_1 and t_o obtained. For the measured data indicated by the jagged lines in figure 7, the smooth lines represent the fitted profiles (7.2). The respective numerical values of p'_p/p_0, c_1, c_2, t_o, ω_0, $\tanh(c_1t_o)$ ($\equiv\sigma$), $\mathscr{A}$, α_1, α_2 and θ_o are tabulated in each row of table 2. Although ω_0 is meaningless in the case with no array, this value at 25.0 °C is used as the reference to make the profile and the parameters dimensionless. To obtain $\mathscr{A}$ as well, use is made of the value of $\kappa = 0.198$.

The initial-value problem thus posed is solved by integrating (2.5) and (2.6) numerically along the 'characteristics' defined by $\mathrm{d}\theta/\mathrm{d}X = -f$ (see Sugimoto 1991, 1992). Numerical values of the parameters δ_R and δ_r are given in table 3. Each

Profile	p'_p/p_0	$c_1\,(\mathrm{s}^{-1})$	$c_2\,(\mathrm{s}^{-2})$	$t_\mathrm{o}\,(\mathrm{ms})$	$\omega_0/2\pi\,(\mathrm{Hz})$	σ	$\mathscr{A}$	α_1	α_2	θ_o
(a)	0.11281	1395.9	34707	1.2169	242.1	0.9352	1.009	0.9177	0.01500	1.851
(b)	0.10366	1541.4	35458	1.4390	242.0	0.9766	0.9081	1.014	0.01534	2.188

TABLE 2. Parameter values for fitting the initial profiles at $x = 0.4$ m shown in figures 7(a) and 7(b) with the functions (7.2) and (7.3).

Case	$T_0\,^\circ\mathrm{C}$	$p_0\,\mathrm{MPa}$	$a_0\,(\mathrm{m\,s}^{-1})$	$\omega_0/2\pi\,(\mathrm{Hz})$	$\nu\,(10^{-4}\,\mathrm{m}^2\,\mathrm{s}^{-1})$	Pr	C	δ_R	δ_r
N	25.0	0.1007	346.8	—	0.1561	0.7089	1.477	0.03777	—
W	24.8	0.1010	346.6	242.0	0.1556	0.7090	1.477	0.03759	0.05866

TABLE 3. Experimental conditions and the values of the material constants and the parameters δ_R and δ_r where N and W stand for the cases without and with the array, respectively.

row shows the respective experimental conditions for cases designated by N and W, where N and W stand for the cases with no array and with the array, respectively. The material constants in each case are evaluated by using the formulae in the Appendix.

7.2. *Results in the case with no array*

First, the evolution from the profile in figure 7(a) is simulated by solving (2.5) without the term $\partial g/\partial\theta$. The values of the parameters associated with the initial profile are tabulated in table 2 while the experimental condition and the values of the constants are given in table 3 in the row designated by Case N. The profiles simulated are compared to those measured at $x = 5.2$ m. Denoting the distance between the points at $x = x_\mathrm{I} = 0.4$ m and $x = 5.2\,\mathrm{m} \equiv x_\mathrm{M}$ by l_M (=4.8 m), the point $x = x_\mathrm{M}$ corresponds to X_0 ($=\kappa\omega_0 l_\mathrm{M}/2a_0$) for the pulse labelled 0 in figure 8. For the pulses labelled n ($n \geqslant 1$), the value of $x - x_\mathrm{I}$ in X and θ is taken to be a distance with $2nl$ added on l_M, where l is 10.654 m, so that X corresponds to X_n ($=X_0 + n\kappa\omega_0 l/a_0$). Note that ω_0/a_0 is determined by geometry alone and independent of temperature. Thus it follows that $X_0 = 2.086$, $\kappa\omega_0 l/a_0 = 9.258$ and $X_n = 2.086 + 9.258n$.

Figure 13 shows the temporal profiles of p'/p_0 simulated at $X = X_n$ ($n = 0, 1, 2, \ldots, 5$), respectively, in (a) to (f) as smooth lines where the abscissa is reverted to the dimensional retarded time θ/ω_0. These profiles at $X = X_n$ are compared with those labelled n in figure 8. Transforming the time for the abscissa in figure 8 into the retarded time $t - (l_\mathrm{M} + 2nl)/a_0$, the profiles labelled n ($n = 0, 1, 2, \ldots, 5$) are redrawn in figure 13(a) to figure 13(f) as jagged lines. It is found that both profiles resemble each other but the measured ones are delayed behind the simulated ones. This is due to the phase lag on reflection. When two shocks collide with each other, they are subjected to phase lag but there is no distortion in profiles (Tatsumi & Tokunaga 1974). Since reflection may be replaced by head-on collision of two identical shocks, the above result is consistent qualitatively, though Tatsumi & Tokunaga (1974) take account of the diffusive effect but no account of the boundary-layer effects.

Let us examine the shock in detail. Figure 14 displays the variations of the shock strength $[p']$, i.e. the jump in the pressure, relative to p_0 with respect to X. The solid line represents the numerical results where the shock formation occurs at $X = 10.21$. The experimental data marked by the dots are measured from the profiles in figure 8 at $x = 5.2$ m, the label corresponding to the pulse in the figure. For the data labelled n

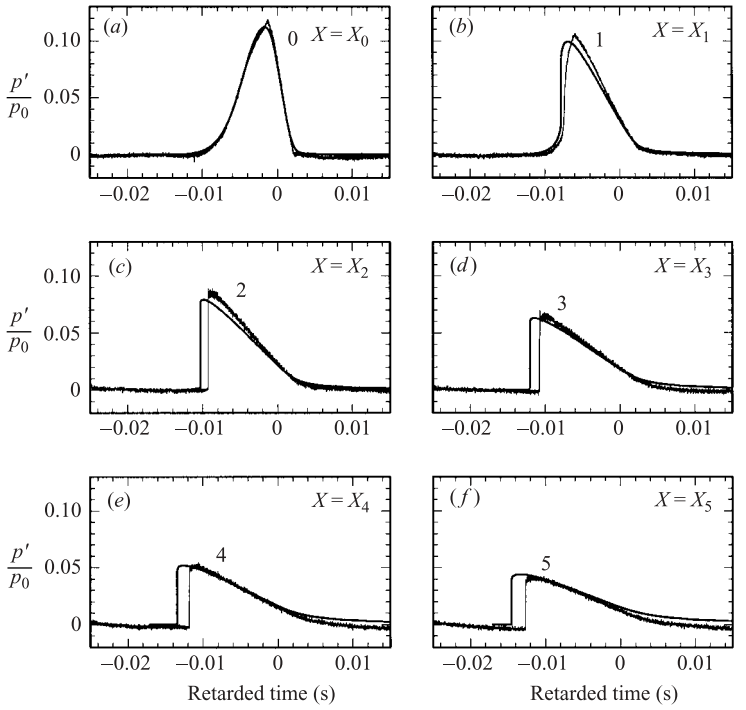

FIGURE 13. Comparison of the temporal profiles of the excess pressure p'/p_0 simulated at $X = X_0, X_1, \ldots, X_5$ and measured at $x = 5.2$ m where the smooth and jagged lines represent the simulated and measured profiles, respectively, and the retarded time measures θ/ω_0 for the simulation and $t - (l_M + 2nl)/a_0$ for the pulse labelled n ($n = 0, 1, 2, \ldots, 5$) in figure 8.

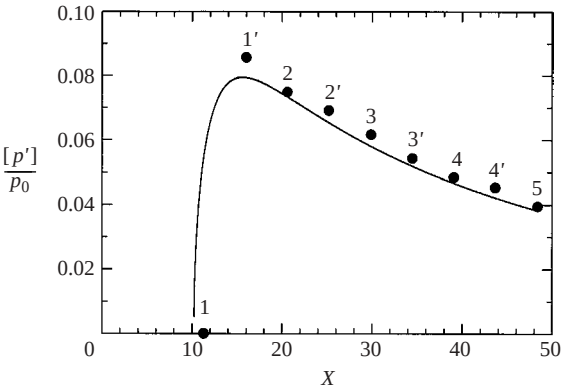

FIGURE 14. Comparison of the shock strength in the tube with no array where the solid line represents the calculation and the dots indicate the data measured from the profiles in figure 8, n and n' ($n = 1, 2, \ldots, 5$) corresponding to the pulses there, and X is calculated by taking the added distance $l_M + 2nl$ for the data labelled n and $l_M + 2l'_M + 2nl$ for the ones labelled n', respectively, $l'_M = x_E - x_M = 5.4$ m.

($n = 1, 2, \ldots, 5$), the value of $x - x_I$ in X is taken to be the added distance $l_M + 2nl$, while for the ones labelled n', the added distance is taken as $l_M + 2l'_M + 2nl$, l'_M being the distance $x_E - x_M = 5.4$ m. The experimental data, except for that of the largest strength, are found to fit well with the theory, though they are subject to the phase

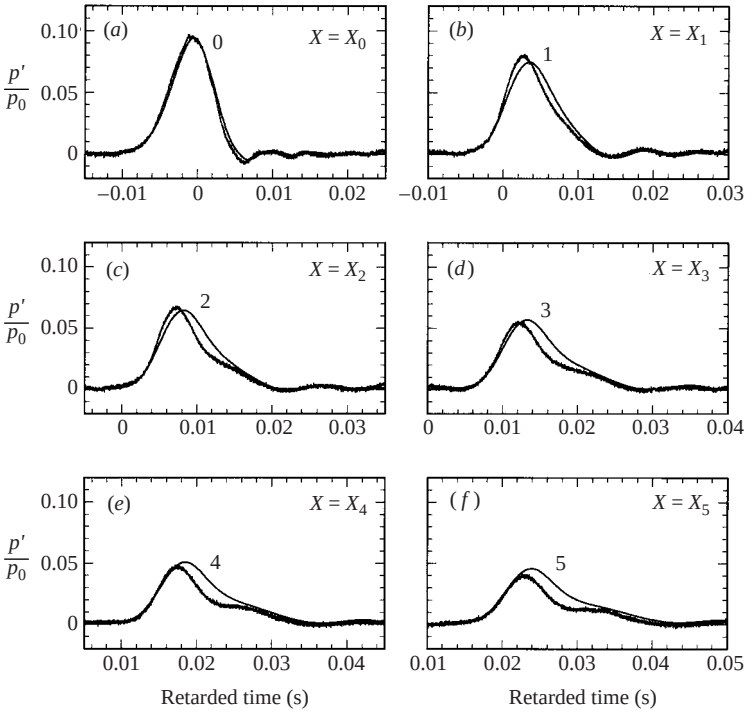

FIGURE 15. Comparison of the temporal profiles of the excess pressure p'/p_0 simulated at $X = X_0, X_1, \ldots, X_5$ and measured at $x = 5.2\,\mathrm{m}$ where the smooth and jagged lines represent the simulated and measured profiles, respectively, and the retarded time measures θ/ω_0 for the simulation and $t - (l_\mathrm{M} + 2nl)/a_0$ for the pulse labelled n ($n = 0, 1, 2, \ldots, 5$) in figure 9.

lag. It is conjectured that the discrepancy between the data of the largest strength and the theory might result from the fact that the initial profile measured in figure 7(a) is not well approximated by the fitted function (7.3) in the vicinity of the peak. Making allowances for this and the phase lag, it may be said that the experimental results are simulated quantitatively very well. Thus validity of (2.6) without $\partial g/\partial\theta$ is justified.

7.3. *Results for the case with the array of resonators*

Next we solve the initial-value problem of (2.5) and (2.6) subject to the initial condition (7.3) corresponding to the pressure profile in figure 7(b). The fitting values for the profile are tabulated in table 2, while the experimental condition is given in table 3 in the row designated by Case W. Figure 15 compares the results of simulation with those measured at $x = 5.2\,\mathrm{m}$. The temporal profiles of p'/p_0 simulated at $X = X_n = 2.086 + 9.258n$ ($n = 0, 1, 2, \ldots, 5$) are depicted in figure 15(a) to figure 15(f), respectively, as smooth lines where the abscissa measures the dimensional retarded time θ/ω_0. The corresponding measured profiles are indicated by the jagged lines where the retarded time is taken as $t - (l_\mathrm{M} + 2nl)/a_0$ for the pulse labelled n. It is found that the measured profiles are well simulated, but they are subject to a phase lead this time. This is conjectured to be brought about by reflection at both ends. For head-on collision of two identical solitons, it is known that they are subjected to a repulsive force so that the phase lead occurs (Oikawa & Yajima 1973). Except for

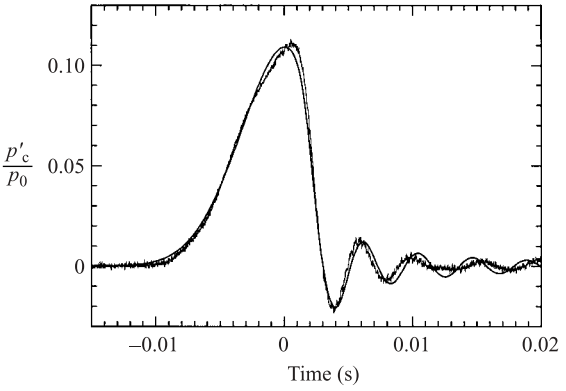

FIGURE 16. Temporal profiles of the excess pressure p'_c/p_0 calculated from the solution (2.6) with $f = F$ fitted by (7.3) for the profile in figure 7(*b*) and measured in the cavity at $x = 0.425$ m where the smooth and jagged lines represent the calculated and measured profiles, respectively.

the phase lead, the decaying behaviour and emergence of an oscillatory tail is well captured quantitatively in the simulations. In figure 15(*c*) to figure 15(*f*), emergence of a small hump on the right-hand side of the peak is also reproduced.

Next let us check the pressure in the cavity. In particular, it is interesting to examine the initial profile of g. Is it really determined by a solution to (2.6) with $f = F$? To this end, the experiment to measure the pressure in the tube at $x = 0.4$ m and in the cavity at $x = 0.425$ m is repeated because there is no resonator at $x = 0.4$ m. The experimental condition is the same as Case W in table 3 except for temperature: $T_0 = 24.7\,^\circ$C. The pressure profile in the tube at $x = 0.4$ m is seen to be identical to the one in figure 7(*b*) and no difference can be found with the naked eye. In fact, the profile can be fitted by the same parameters as for profile (*b*) in table 2. Figure 16 shows the comparison of the excess pressure p'_c/p_0 calculated from the solution (2.6) with $f = F$ fitted by (7.3) and measured at $x = 0.425$ m where the smooth and jagged lines represent the calculated and measured profile, respectively. The calculated profile is the initial profile of g at $X = 0$. But this is different, strictly speaking, from the one at $x = 0.425$ m. This point corresponds to $X = \Delta X$ ($=0.025\kappa\omega_0/2a_0 \approx 0.01$) where a_0 and ω_0 are measured in units of $\mathrm{m\,s^{-1}}$ and $\mathrm{s^{-1}}$, respectively. In the results of the simulation, however, no difference is seen in the figure. It is gratifying to find that both profiles agree quantitatively with each other very well. Two oscillations in the tail are well reproduced. This confirms the validity not only of (2.6) alone but also of both (2.5) and (2.6).

Finally the pressure profiles in the cavity at the point $x = 5.225$ m are checked. To this end, the experiment is again repeated to measure the pressure in the tube at $x = 0.4$ m and the pressure in the cavity at $x = 5.225$ m. The experimental condition is the same except for temperature: $T_0 = 24.6\,^\circ$C. The position at $x = 5.225$ m for the pulse labelled n corresponds to $X = X_n + \Delta X$. Here ΔX is also neglected. Figure 17 compares the profiles of p'_c/p_0 calculated from the solutions of g at $X = X_n$ ($n = 0, 1, 2, \ldots, 5$), and measured at $x = 5.225$ m, as smooth and jagged lines, respectively, where the abscissa is reverted to the dimensional retarded time θ/ω_0 for the simulation and $t - (l_M + 2nl)/a_0$ for the pulse labelled n. In this case as well, the measured profiles are well simulated except for the phase lead. In figure 17(*b*) and figure 17(*c*), the measured peak pressure is slightly higher than that simulated. But

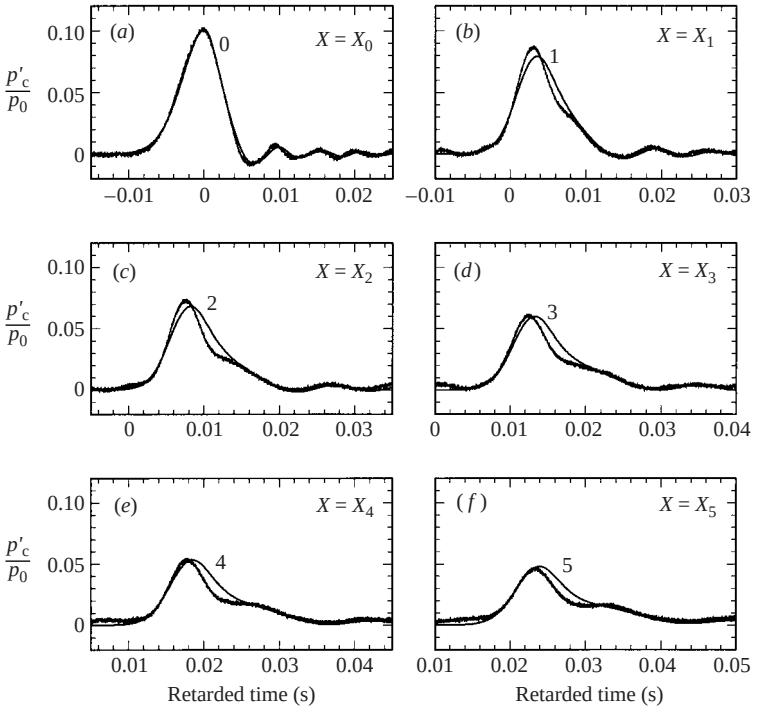

FIGURE 17. Comparison of the temporal profiles of the excess pressure p'_c/p_0 simulated at $X = X_0, X_1, \ldots, X_5$ and measured in the cavity at $x = 5.225$ m where the smooth and jagged lines represent the simulated and measured profiles, respectively, and the retarded time measures θ/ω_0 for the simulation and $t - (l_M + 2nl)/a_0$ for the pulse labelled n (=0, 1, 2, ..., 5).

the decaying behaviour is well described quantitatively. Thus it is revealed that (2.5) and (2.6) are reliable enough to simulate real evolutions.

8. Discussion

Lossy effects on the deformation of the profile are discussed in this section. First, the lossless evolution from profile (*b*) in table 2 is solved by ignoring the boundary-layer effects and $\kappa N/2$ in (2.5) and (2.6). Since the term $\kappa N/2$ is mainly contributed by the jet loss, this term may be called simply the jet loss. Figure 18(*a*) shows the results of simulations for p'/p_0 at $X = 0, X_1, X_2, \ldots, X_5$. It is surprising to find that the peak becomes higher as it evolves. For the profiles at $X = X_2, X_3, X_4$ and X_5, the solitary waves having the corresponding peak values are drawn as broken lines. The profile at $X = X_5$ is almost identical to the solitary wave, though an oscillatory tail develops.

Next only the boundary-layer effects are taken into account and the same initial-value problem is solved. Figure 18(*b*) depicts the results of simulations where the broken lines represent the solitary waves. The boundary-layer effects give rise to significant attenuation of the peak value and retardation in propagation. Nevertheless the profile at $X = X_5$ is well approximated by the solitary wave, but the tail becomes thicker. Further, when the full equations are solved, the results are shown in figure 18(*c*). The jet loss gives rise to further decrease in the peak value and

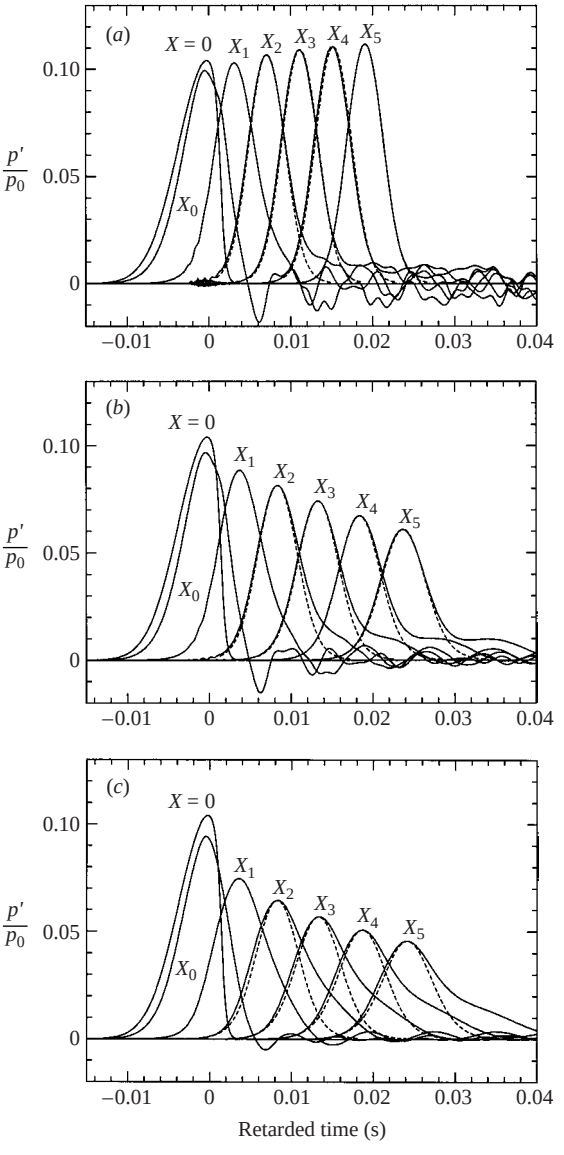

FIGURE 18. Effects of the boundary layers and the jet loss on the evolution from profile (*b*) in table 2 where the temporal profiles of p'/p_0 at $X = 0, X_1, X_2, \ldots, X_5$ versus the retarded time θ/ω_0 are shown for (*a*) without both the boundary-layer effects and the jet loss, (*b*) with the boundary-layer effects but without the jet loss, and (*c*) with all effects included, and the broken lines represents the fitted solitary waves.

retardation. The profiles on the left-hand side of the peak remain close to the solitary waves. But a hump rather than the tail apears on the right-hand side. Below the half-value the profiles become asymmetric. This may explain why the direct check of the half-width has led to good agreements with the theory in spite of the existence of the lossy effects.

These results also suggest improvements of the geometry of the tube and the resonators and also of experimental conditions. To reduce the boundary-layer effects,

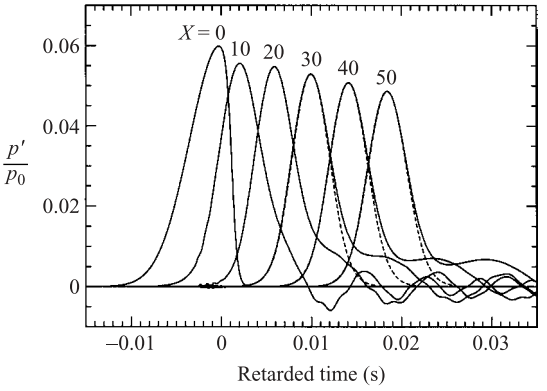

FIGURE 19. Simulation of the evolution in the tube with the array of resonators with $\kappa = 0.0991$ and the boundary-layer effects and the jet loss reduced by remodelling the resonators so as to double B, L and d and by increasing the equilibrium pressure to 10 MPa at $T_0 = 300$ K where the initial profile (7.3) with $\mathscr{A} = \alpha_1 = 1$, $\alpha_2 = 0.015$ and $\theta_o = 2$ is imposed at $X = 0$. The solid lines represent the numerical simulations with the solitary waves as broken lines, the dimensionless distance 10 in X corresponding to 45 m physically.

use of a wider tube and a throat is obviously preferable. Besides this, use of a higher equilibrium pressure p_0 is also desirable. But the jet loss cannot be reduced by these alterations, since it is determined solely by the specific geometry of the resonator. For the resonator used, the coefficient of the jet loss $\kappa V/(\gamma + 1)BL_e$ in (2.6) takes the large value 2.50. To reduce this, a wide and longer throat is required. If B and L are taken double the size, the coefficient becomes a quarter of the present value with natural angular frequency almost unchanged.

In the light of these results, we finally simulate the evolution in the present tube by using the resonators remodelled to have doubled values of B and L and also by reducing the value of κ to half, i.e. 0.0991, by taking double the axial spacing of resonators. Then $\kappa V/(\gamma + 1)BL_e$ is reduced to 0.304. In addition, p_0 is set to be 10 MPa at $T_0 = 300$ K. The material constants in this case are given separately in the last paragraph of the Appendix. The equation of state for the ideal gas is assumed to be valid for small changes around 10 MPa (Hilsenrath *et al.* 1960). Using those data, it follows that $\omega_0/2\pi = 263.4$ Hz, $\delta_R = 8.570 \times 10^{-3}$ and $\delta_r = 4.185 \times 10^{-3}$. Thus the effect of the boundary layers is considerably suppressed, but that of the jet loss may be even larger.

Assuming the profile (7.3) with $\mathscr{A} = 1$, $\alpha_1 = 1$, $\alpha_2 = 0.015$ and $\theta_o = 2$ in view of the initial profile (*b*) in table 2, figure 19 shows the profiles of p'/p_0 as the solid lines up to $X = 50$ in steps of 10 with the solitary waves as the broken lines having the corresponding peak values at $X = 30, 40$ and 50. As X increases, the initial pulse evolves into the solitary wave except for the tail. The peak value does not change much once the pulse has almost approached the solitary wave. For $\kappa = 0.0991$, dimensionless distance 10 corresponds to 45 m. Thus the pulse can be propagated with little attenuation over a much longer distance than in the present experiments. This is indeed a 'gas-dynamic' solitary wave with very high peak pressure, although the adjective 'acoustic' gives an impression of very small disturbances. Such a solitary wave may find applications in thermoacoustic problems (Sugimoto & Tsujimoto 2002).

9. Conclusions

This paper has examined the existence of the acoustic solitary wave by performing both experiments and numerical simulations to strengthen the conclusions in the previous work (Sugimoto *et al.* 1999). The experimental apparatus has been greatly improved by using a newly designed piston driver to launch a plane pressure pulse, and also extending the tube length from 7.4 m to 10.6 m. The methods and results of the experiments have been described in detail. On the other hand, the simulations have been carried out in parallel by solving the initial-value problems of the nonlinear wave equations (2.5) and (2.6). The existence of the solitary wave has been checked in two ways. One is the direct check of the profiles and the propagation speeds of the measured pulses against the theory. This is simply a re-examination of the previous results. This check has reconfirmed existence of the solitary wave.

The other is an indirect but intrinsic check by examining the validity of the basic equations suggesting the existence of the solitary waves. Taking account of all lossy effects, the evolution observed has been simulated numerically. The evolution in the tube with no array has also been checked because no experimental verification of the theory has so far been made. It is revealed that the shock formation and the boundary-layer effects are well reproduced in comparison to the experimental results. The quadratically nonlinear wave equation (2.5) without $\partial g/\partial\theta$, originally for unidirectional propagation, is found to be applicable even to propagation in the tube of finite length if some phase lag on reflection is allowed.

For the case with the array of resonators as well, it is revealed that the evolution in the experiments is simulated quantitatively well if a phase lead is allowed this time. In particular, the lossy effects are well reproduced. As the peak pressure becomes higher, the jet loss comes into play. It yields a hump and makes the profile asymmetric. But when the jet loss becomes primary, the solitary-wave solution (2.10) becomes invalid. Since the jet loss in the resonators used turns out to be very large, the solitary wave near the limiting one is difficult to generate in the present tube. Even so, it has been proven that nonlinear wave equations (2.5) and (2.6) can still describe the real evolution accurately in the tube of finite length. Now that the validity of the equations is established, it can be concluded that the acoustic solitary wave exists in the lossless limit.

The authors acknowledge the comments by reviewers for improvement of the manuscript, and also assistance of Messrs S. Deguchi and Y. Masuda in doing the experiments. This work has been supported by the Grants-in-Aids from the Japan Society of Promotion of Science and also from The Mitsubishi Foundations, Tokyo, Japan.

Appendix. Evaluation of material constants of air

This Appenidix is devoted to summary of the formulae necessary to evaluate the material constants of air in the main text. All formulae are well known and documented in books, e.g. see Pierce (1991, pp. 28–29 and 513–514).

Air is assumed to obey the equation of state of an ideal gas with gas constant $\mathscr{R} = 2.870 \times 10^2\,\mathrm{J\,kg^{-1}\,K^{-1}}$. As the sound speed a_0 is given by $\sqrt{\gamma p_0/\rho_0}(=\sqrt{\gamma \mathscr{R} T_0})$, we use the formula expanded around $T_0 = 273.16\,\mathrm{K}$:

$$a_0 = 331.5 + 0.61 \times (T_0 - 273.16)\,\mathrm{m\,s^{-1}}, \tag{A 1}$$

where T_0 is measured in the absolute temperature units (K) and the effect of humidity is ignored. The specific heat c_p is taken to be the constant $1.007\,\mathrm{kJ\,kg^{-1}\,K^{-1}}$, while the ratio of specific heats γ is assumed independent of temperature and is set equal to 1.402.

The viscosity and the thermal conductivity are functions of temperature only. The viscosity μ at temperature T_0 is evaluated by Sutherland's formula:

$$\frac{\mu}{\mu_C} = \left(\frac{T_0}{T_C}\right)^{3/2} \frac{T_C + T_S}{T_0 + T_S}, \tag{A 2}$$

where $\mu_C = 1.846 \times 10^{-5}\,\mathrm{kg\,m^{-1}\,s^{-1}}$ and $T_S = 110.4\,\mathrm{K}$ for $T_C = 300\,\mathrm{K}$. The thermal conductivity k_T at T_0 is evaluated by the empirical formula

$$\frac{k_T}{k_{TC}} = \left(\frac{T_0}{T_C}\right)^{3/2} \frac{T_C + T_A \exp(-T_B/T_C)}{T_0 + T_A \exp(-T_B/T_0)}, \tag{A 3}$$

where $k_{TC} = 2.624 \times 10^{-2}\,\mathrm{W\,m^{-1}\,K^{-1}}$, $T_A = 245.4\,\mathrm{K}$ and $T_B = 27.6\,\mathrm{K}$.

The kinematic viscosity ν at T_0 is obtained by dividing μ by the density ρ_0 at equilibrium where ρ_0 is calculated by the equation of state: $\rho_0 = p_0/\mathscr{R}T_0$. With ν and $Pr(=\mu c_p/k_T)$ in C known, and ω_0 dependent on a_0, δ_R and δ_r are evaluated. Their values used in the simulations are tabulated in table 3.

Finally the data of the material constants at $T_0 = 300\,\mathrm{K}$ and $p_0 = 10\,\mathrm{MPa}$ are presented. According to JSME (1994), ρ_0, c_p, k_T and γ takes the values $1.169 \times 10^2\,\mathrm{kg\,m^{-3}}$, $1.163\,\mathrm{kJ\,kg^{-1}\,K^{-1}}$, $3.178 \times 10^{-2}\,\mathrm{W\,m^{-1}\,K^{-1}}$ and 1.568, respectively. Thus it follows that $a_0 = 369.4\,\mathrm{m\,s^{-1}}$, $Pr = 0.7491$, $C = 1.656$ and $\nu = 1.751 \times 10^{-7}\,\mathrm{m^2\,s^{-1}}$, respectively.

REFERENCES

Chester, W. 1964 Resonant oscillations in closed tubes. *J. Fluid Mech.* **18**, 44–64.

Hellemans, A. 1999 Conjuring a solitary sound wave. *Science* **286**, 2062.

Hilsenrath, J., Hoge, H. J., Beckett, C. W., Masi, J. F., Benedict, W. S., Nuttall, R. L., Fano, L., Touloukian, Y. S. & Woolley, H. W. 1960 *Tables of Thermodynamic and Transport Properties of Air, Argon, Carbon Dioxide, Carbon Monoxide, Hydrogen, Nitrogen, Oxygen, and Steam.* Pergamon.

Japan Society of Mechanical Engineers 1994 *Thermophysical Properties of Fluids.* Maruzen, pp. 163–191 (in Japanese).

Keller, J. J. 1981 Propagation of simple, non-linear waves in gas-filled tubes with friction. *Z. Angew. Math. Phys.* **32**, 170–181.

Oikawa, M. & Yajima, N. 1973 Interactions of solitary waves – A perturbation approach to nonlinear systems. *J. Phys. Soc. Japan* **34**, 1093–1099.

Physical Review Focus 1999 The sound of solitary wave. *Am. Phys. Soc.* http://focus.aps.org/v4/st24.html, Nov.15.

Pierce, A. D. 1991 *Acoustics: An Introduction to Its Physical Principles and Applications.* Acoustical Society of America.

Sugimoto, N. 1991 Burgers equation with a fractional derivative; hereditary effects on nonlinear acoustic waves. *J. Fluid Mech.* **225**, 631–653.

Sugimoto, N. 1992 Propagation of nonlinear acoustic waves in a tunnel with an array of Helmholtz resonators. *J. Fluid Mech.* **244**, 55–78.

Sugimoto, N. 1995 The generation of an acoustic soliton and soliton tube. *Proc. Estonian Acad. Sci. Phys. Math.* **44**, 56–72.

Sugimoto, N. 1996 Acoustic solitary waves in a tunnel with an array of Helmholtz resonators. *J. Acoust. Soc. Am.* **99**, 1971–1976.

Sugimoto, N. 2001 Emergence of an acoustic shock wave in a tunnel and a concept of shock-free propagation. In *Noise and Vibration from High-Speed Trains* (ed. V. V. Krylov), pp. 213–247. Thomas Telford Publishing.

Sugimoto, N., Masuda, M., Ohno, J. & Motoi, D. 1999 Experimental demonstration of generation and propagation of acoustic solitary waves in an air-filled tube. *Phys. Rev. Lett*. **83**, 4053–4056.

Sugimoto, N. & Tsujimoto, K. 2002 Amplification of energy flux of nonlinear acoustic waves in a gas-filled tube under an axial temperature gradient. *J. Fluid Mech.* **456**, 377–409.

Tatsumi, T. & Tokunaga, H. 1974 One-dimensional shock turbulence in a compressible fluid. *J. Fluid Mech.* **65**, 581–601.

Weiss, P. 1999 Single-wave sounds streak through air. *Science News* **156**, 327.